

1 **GRAIN FRICTION CONTROLS CHARACTERISTICS OF**
2 **SEISMIC CYCLE IN GRANULAR FAULT GOUGE;**
3 **IMPLICATIONS FOR FAULT PARTICLE ROUGHNESS**

4 **Authors:**

5 **I. Omid Dorostkar^{1,2,*}**

- 6 1. Chair of Building Physics, Department of Mechanical and Process
7 Engineering, Swiss Federal Institute of Technology Zurich (ETH Zurich),
8 Stefano-Franscini-Platz 5, CH-8093 Zurich, Switzerland
9 2. Department of Civil, Environmental and Geomatic Engineering, Swiss
10 Federal Institute of Technology Zurich (ETH Zurich), Stefano-Franscini-
11 Platz 5, CH-8093 Zurich, Switzerland

12 *Corresponding author:

13 Email: domid@ethz.ch Phone: +41587654106

14 ID: orcid.org/0000-0002-7758-4919

15 **II. Jan Carmeliet¹**

- 16 1. Chair of Building Physics, Department of Mechanical and Process
17 Engineering, Swiss Federal Institute of Technology Zurich (ETH Zurich),
18 Stefano-Franscini-Platz 5, CH-8093 Zurich, Switzerland

19 Email: cajan@ethz.ch

20
21 **This is a non-peer reviewed preprint submitted to EarthArXiv. The**
22 **manuscript is submitted to Journal of Geophysical Research (JGR), Solid**
23 **Earth for possible publication.**

26 **Abstract:**

27 In this paper, we study the effect of particle roughness approximated by the inter-
28 particle friction coefficient on the characteristics of seismic cycles. Our discrete
29 element simulations show that the stick-slip frictional strength and dilation of the
30 fault gouge, as well as their variability, nonlinearly increase with the particle
31 roughness (inter-particle friction coefficient) but at high particle roughness saturate.
32 By statistical analyses on a large number of slip events, we find that the average
33 recurrence time and its variability decreases with particle roughness. A rougher fault
34 shows a more complex nucleation phase and more frequent energy releases in the
35 kinetic energy signal. We find that the rougher fault on average shows more small
36 slip events compared to smoother fault but also contains a limited number of
37 extreme events. The fault gouge with higher particle surface roughness shows higher
38 stored potential energy and stronger particle-particle contact forces. Our pseudo
39 acoustic emission analysis, based on the monitoring of the velocity signal of particles,
40 shows higher temporal and more spatially distributed acoustic emissions for fault
41 gouge with higher particle surface roughness. Our findings in this study show that
42 roughness at micro-scale plays an important role in nucleation and rupture process
43 of earthquakes, similar to conditions where no granular gouge was considered. Our
44 results in this study are consistent with previous numerical and experimental works
45 and complete them by focusing on micromechanics of fault damage zone, showing
46 how numerical models and in particular discrete element simulations can help
47 enhance our understanding from fault mechanics.

48 **Keywords:** friction, roughness, stick-slip, granular materials, fault gouge, fault
49 mechanics

50 **1- Introduction**

51 The stability and slip behavior of natural faults and their relation with fault properties
52 and in particular, their surface roughness, have been under debate during last years.
53 The fault roughness spans from microns to tens of kilometers and can be measured
54 using different methods. Brodsky et al. [2016] quantified the slip surface roughness
55 and found that fault surface is rougher at small scales than large ones and that the
56 scale dependence of roughness implies yielding of asperities at all scales [*Brodsky et*
57 *al., 2016*]. Using three independent scanner devices, Candela et al. [2012]
58 characterized the roughness of fault surfaces by a single anisotropic self-affine
59 description [*Candela et al., 2012*]. The fault surface roughness has been evaluated also
60 by measurements on exhumed faults [*Renard et al., 2006; Sagy et al., 2007; Candela et*
61 *al., 2009; Bistacchi et al., 2011; Brodsky et al., 2011*].

62 At field scale, the fault roughness is suggested to control the stress drop and slip
63 distribution during earthquakes [*Bouchon et al., 2010; Candela et al., 2011a; Candela et*
64 *al., 2011b*]. The maturity and roughness level of nearby faults are also reported to
65 influence seismic hazard associated with hydraulic fracturing [*Kozłowska et al., 2018*].
66 A recent report shows that the seafloor in front of large earthquakes is generally
67 smoother than in areas where no large earthquakes have occurred [*Rijsingen et al.,*
68 *2018*]. In their review paper on field scale observation regarding fault creep caused
69 by subduction of rough seafloor relief, Wang & Bilek [2014] reported lack of
70 evidence for rough faults to be more strongly locked, while creeping is observed for
71 both smooth and rough faults [*Wang & Bilek, 2014*].

72 It is barely feasible to study the relation of roughness and seismicity in nature. At lab
73 scale, experimental studies showed that roughness promotes a larger nucleation
74 segment [Obnaka & Shen, 1999; Obnaka, 2003]. The study by Goebel et al. [2014]
75 showed that, as the shearing of an experimental sample advances, there exists a rapid
76 spatial decay of acoustic emission events during following inter-slip periods, that is
77 an intimation of decreasing fault zone complexity and fault surface roughness [Goebel
78 et al., 2014a]. In experiments, the smoother faults are proposed to show super-shear
79 ruptures as roughness controls the velocity of rupture propagation [Xia et al., 2004;
80 Schubnel et al., 2011]. The topology and fault structure influence the spatial and
81 temporal distribution of small and large earthquakes. Using laboratory experiments,
82 Goebel et al. [2017] showed that more mature, smoother faults produce localized
83 seismicity, smoother stress fields, and lower b-values (the measure for the relative
84 abundance of the strong to the weak earthquakes based on the Gutenberg–Richter
85 law), and that the acoustic emission statistics during stick-slip are strongly influenced
86 by fault roughness [Goebel et al., 2017]. In their recent review on scaling of fault
87 roughness and its implications for earthquake mechanics, Renard & Candela [2017]
88 emphasized on the open question of fault roughness at small scales (below the
89 millimeter scale) and its possible implications for seismic and aseismic slip [Renard &
90 Candela, 2017].

91 Numerical simulations have been also used to study the effect of roughness on
92 mechanics and nucleation of slip events as well as heterogeneity of stress distribution
93 and dissipation due to fault zone roughness [Chester & Chester, 2000; Dieterich & Smith,

94 2009; *Angheluta et al., 2011; Dunham et al., 2011; Bruhat et al., 2016; Tal & Hager, 2018;*
95 *Tal et al., 2018*]. Previous research using 2-D discrete element method (DEM)
96 showed that the fault roughness can control the slip style from stick-slip to stable
97 sliding [*Fournier & Morgan, 2012*]. Using 3-D DEM, Rathbun et al. [2013] found that,
98 in stable sliding regime, roughness and thus coupling of a fault to the gouge zones
99 influences the number of sliding contacts controlling the critical slip distance [*Marone*
100 *& Kilgore, 1993; Rathbun et al., 2013*]. Using large-scale numerical simulations, Zielke
101 et. al [2017] suggested that, besides stress drop and rupture dimension, the
102 earthquake moment release and its recurrence probability is dependent also on
103 surface roughness [*Zielke et al., 2017*]. In a new numerical study, Pierre et al. [2018]
104 showed, without appealing to complex friction rheology, that a simple geometrical
105 complexity with two overlapping faults give rise to both slow and fast slip events
106 [*Pierre et al., 2018*].

107 Faults at their core are usually characterized by a granular gouge layer created by
108 wear, comminution and other frictional processes, as observed in nature [*Engelder,*
109 *1974; Shimamoto, 1979; Chester et al., 1985; Chester & Logan, 1986; Marone et al., 1990;*
110 *Chester & Chester, 1998; Cashman & Cashman, 2000; Chester & Chester, 2000; Faulkner*
111 *et al., 2003; Heermance et al., 2003; Cashman et al., 2007; Zoback et al., 2010*].
112 Characteristics of slip events in laboratory stick-slip experiments including stress
113 drop, pre-seismic friction, recurrence time, granular layer compaction etc. have been
114 studied widely for different loading configurations and particle properties [*Dieterich*
115 *& Kilgore, 1994; Marone, 1998a; Karner & Marone, 2000; Mair et al., 2002; Brantut et al.,*

116 2008; Rathbun & Marone, 2010; Haines et al., 2014; Rosenau et al., 2017], where the
117 frictional strength and stability of a sheared granular zone are found sensitive to grain
118 shape, particle size distribution and their evolution [Mair et al., 2002; Anthony &
119 Marone, 2005].

120 Despite its dependency on many factors, generally the contact friction coefficient
121 increases with surface roughness parameters [Biegel et al., 1989; Ivković et al., 2000; Park
122 & Song, 2009]. In this study, we systematically vary the inter-particle friction
123 coefficient as a proxy for particle roughness in a granular fault gouge, as the presence
124 of granular fault gouge is neglected in most of the previous studies on fault
125 roughness. We focus on stick-slip dynamics and the effect of particle roughness on
126 characteristics of seismic cycles to answer the following question; “what is the effect
127 of inter-particle roughness on the slip size distribution and inter-event time of seismic
128 cycles in a fault with granular fault gouge?”. To this end, we perform 3-D DEM
129 simulations recording hundreds of slip events for statistical analyses provided by the
130 advantage of numerical simulations. We also study the evolution of elastic strain
131 energy (potential energy [Dorostkar, 2018; Dorostkar & Carmeliet, 2018]), kinetic
132 energy, and the micromechanics of slip events and explain the macro-scale response
133 of fault with grain-scale metrics (e.g. [Dorostkar et al., 2017a]). In absence of complex
134 rheological and geometrical granular contact model, we will show that, although our
135 simplified numerical approach does not contain many complexities present in nature,
136 it can yet show similar observations to recent numerical and experimental studies on
137 fault roughness and complete them by statistical analyses using a large quantity of

138 slip events. Our findings in this study will show that roughness at micro-scale level,
139 approximated by inter-particle friction coefficient, may play a similar role in
140 mechanics of earthquakes as roughness of fault blocks' surface in absence of fault
141 gouge.

142 **2- Model description**

143 Due to particulate nature of granular fault gouge, we use DEM to model gouge
144 grains. In DEM, the equations of motion solved for each particle considering the
145 applied forces are:

$$146 \quad \sum F_p = m \left(\frac{d}{dt} u_p \right), \quad (1)$$

$$147 \quad \sum T_p = I \left(\frac{d}{dt} \omega_p \right), \quad (2)$$

148 where m , I , u_p and ω_p are the mass, the moment of inertia and the translational and
149 angular velocity of particle, respectively. In Eq. (1) and (2), F_p and T_p are the forces
150 and torques acting on particle i owing to particle-particle contacts. In soft sphere
151 DEM, the particle-particle contact allows an overlap between them and the contact
152 law is described by a combination of different rheological elements (spring, dashpot,
153 slider etc.). These elements are at play when particles are in contact. Upon contact
154 loss, there are no contact forces acting between the particles. The process of forming
155 new contacts and contact loss changes the stiffness of the granular system. Particle
156 sliding also changes the shear stiffness. These phenomena introduce a nonlinear
157 strain dependent behavior of the granular material [O'Sullivan, 2011]. The contact
158 nonlinearity is mainly effective at smaller strains, while material nonlinearity arises

159 mainly from a change in the number and the fabric of contacts taking place at larger
160 strains [O'Sullivan, 2011]. Material nonlinearity is recognized to play an important role
161 in the weakening process of granular materials [Johnson & Jia, 2005]. There is a variety
162 of contact laws used in DEM [Di Renzo & Di Maio, 2004], however, in order to
163 capture particle scale nonlinearity, we use the nonlinear Hertzian contact law. In this
164 particle-particle contact law, the spring stiffness and the coefficient of damping are
165 function of particle material properties and the overlap between particles [Hertz,
166 1882; Di Renzo & Di Maio, 2004]. The normal and tangential contact forces are
167 calculated as follows:

$$168 \quad F_{pn} = -k_{pn}\delta\varepsilon_{pn} + c_{pn}\delta u_{pn}, \quad (3)$$

$$169 \quad F_{pt} = \min \left\{ \left| k_{pt} \int_{t_{c,0}}^t \delta u_{pt} dt + c_{pt} \delta u_{pt} \right|, \mu_c F_{pn} \right\}, \quad (4)$$

170 where k_{pn} and k_{pt} are the normal and tangential spring stiffness, c_{pn} and c_{pt} are
171 the normal and tangential damping coefficient, $\delta\varepsilon_{pn}$ is the overlap and δu_{pn} and
172 δu_{pt} are the relative normal and tangential velocities of two particles in contact,
173 respectively. In Eq. (4), the parameter μ_c represents the inter-particle friction
174 coefficient that limits the tangential force. When the tangential contact force between
175 two particles in contact reaches this limit, they start sliding against each other. The
176 integral term in Eq. (4) shows an incremental spring, storing energy based on the
177 relative elastic tangential deformation of the particle surface starting from the
178 moment particles touch each other at $t_{c,0}$. A damping is added to the spring
179 component of the tangential force if the Coulomb criterion is not met [Di Renzo &

180 *Di Maio, 2004; Goniva et al., 2012*]. The spring and damping coefficients are calculated
 181 as follows:

$$182 \quad k_{pn} = \frac{4}{3} Y^* \sqrt{R^* \delta \varepsilon_{pn}}, \quad (5)$$

$$183 \quad k_{pt} = 8 G^* \sqrt{R^* \delta \varepsilon_{pn}}, \quad (6)$$

$$184 \quad c_{pn} = -2 \sqrt{\frac{5}{6}} \times \frac{\ln(r)}{\sqrt{\ln^2(r) + \pi^2}} \times \sqrt{2Y^* \sqrt{R^* \delta \varepsilon_{pn}} m^*}, \quad (7)$$

$$185 \quad c_{pt} = -2 \sqrt{\frac{5}{6}} \times \frac{\ln(r)}{\sqrt{\ln^2(r) + \pi^2}} \times \sqrt{8 G^* \sqrt{R^* \delta \varepsilon_{pn}} m^*}, \quad (8)$$

186 where, r is the restitution coefficient, and Y^* , R^* , G^* and m^* are the equivalent
 187 Young's modulus, radius, shear modulus and mass, respectively, calculated as
 188 follows:

$$189 \quad \frac{1}{Y^*} = \frac{(1-\nu_1^2)}{Y_1} + \frac{(1-\nu_2^2)}{Y_2}, \quad (9)$$

$$190 \quad \frac{1}{G^*} = \frac{2(2-\nu_1)(1+\nu_1)}{Y_1} + \frac{2(2-\nu_2)(1+\nu_2)}{Y_2}, \quad (10)$$

$$191 \quad \frac{1}{R^*} = \frac{1}{R_1} + \frac{1}{R_2}, \quad (11)$$

$$192 \quad \frac{1}{m^*} = \frac{1}{m_1} + \frac{1}{m_2}, \quad (12)$$

193 where subscripts 1 and 2 refer to the two particles in contact and ν is the Poisson's
 194 ratio of the particle.

195 Figure 1 illustrates a granular layer representing a part of a granular fault gouge.
 196 In our model, 8000 spherical particles constitute this layer with particle diameter
 197 ranging 90-150 μm having a uniform, poly-disperse particle size distribution. The
 198 sample size in our simulations is $11 \times 1.5 \times 0.8 \text{ mm}^3$. This sample size is large enough

199 to show proper effect of 3D particle interaction [Ferdowsi, 2014] as well as
200 jamming/unjamming transitions in the granular layer [Marone et al., 2008]. On the
201 sample top and bottom, we employ two corrugated plates with high surface
202 roughness modeled by a friction coefficient of 0.9 between the plates and particles
203 to facilitate the transmission of shear stresses to the granular gouge. This kind of
204 geometry is inspired from the BIAx laboratory earthquake machine using corrugated
205 driving blocks [Marone, 1998a; Rivière et al., 2018]. In this paper, our study is dedicated
206 to influence of the particle roughness of fault gouge material represented by inter-
207 particle friction coefficient on stick-slip behavior. We do not study the effect of
208 characteristics of the corrugated plates e.g. length, depth, etc. on the dynamics of the
209 sheared granular layer, since a detailed analysis showed that change of these
210 characteristics does not alter the dynamic regime. On the front- and back-sides of
211 the sample, we implement frictionless walls with the same elastic properties of
212 particles. This type of interaction between particles and walls are designed to avoid
213 rigid wall boundary conditions. Wall-particle interaction in our DEM model is the
214 same as particle-particle interaction when one particle has an infinite radius. Periodic
215 boundary conditions are applied at the left and right sidewalls representing a long
216 fault gouge in x direction. The periodic boundary conditions allow for large shear
217 displacements, and facilitate recording many slip events to be used for statistical
218 analyses. To prepare the sample, particles are inserted randomly in space descending
219 with an initial velocity of 10^{-2} cm/s. Next, the upper plate is moved downward to
220 apply a confining stress to confine the sample. At this stage, the confining stress

221 increases until the desired confining stress is attained (10 MPa). The position of the
222 upper plate is adapted continuously, as in the lab experiments, in order to maintain
223 the confining stress constant. At constant confining stress, shearing is initiated by
224 moving the bottom plate in x direction with a displacement-controlled mechanism
225 (constant velocity of 600 $\mu\text{m/s}$) until reaching the maximum shear stress, at which
226 point the stick-slip process commences. The particle density is 2900 kg/m^3 that
227 results in an applied time step for DEM calculations of 15×10^{-9} seconds, within the
228 recommended range based on the Rayleigh time. Our DEM calculations remain in
229 the quasi-static regime by controlling the inertial number to be below 10^{-3} [*MiDi*,
230 *2004*; *Sheng et al., 2004*; *Agnolin & Roux, 2007*]. Similar to our previous works
231 [*Dorostkar et al., 2017c*; *Dorostkar et al., 2018*], we use LIGGGHTS [*Goniva et al., 2012*;
232 *Kloss et al., 2012*] to model the granular fault gouge.

233 **3- Results**

234 We show in Fig. 2a and 2b the evolution of macroscopic friction and gouge thickness,
235 respectively, for three different inter-particle frictions of 0.1, 0.5 and 0.9 during the
236 stick-slip dynamics. The macroscopic friction is defined as the ratio of shear stress
237 to normal stress (confining stress) on the driving block and the gouge thickness
238 represents the measurement in z direction of Fig. 1. Figure 2c shows with higher
239 resolution the shaded area in Fig. 2a. The macroscopic friction (or shear stress since
240 the confining stress is kept constant) increases nonlinearly reaching to a critical state
241 where micro-slips take place followed by a major slip event. The average macroscopic
242 friction increases nonlinearly with the inter-particle friction coefficient: at low inter-

243 particle coefficients (0.1 to 0.5), the macroscopic friction coefficient increases much
244 more compared to high inter-particle coefficients (0.5 and 0.9). A similar behavior
245 can be observed for the gouge thickness (Fig. 2b).

246 We perform long simulations for inter-particle friction coefficients between 0.1 -
247 1 and measure the average macroscopic friction over all stick and slip phases (Fig.
248 3a). We observe that the gouge strength represented by macroscopic friction
249 increases nonlinearly with inter-particle friction and saturates at around $\mu_c = 0.9$ to
250 1. A similar behavior is observed for gouge thickness (Fig. 3b). The standard
251 deviations in macroscopic friction signal and gouge thickness are found to increase
252 with increasing inter-particle friction coefficient (Fig. 3a and 3b). We calculate the
253 slip recurrence time for slip events with a drop in macroscopic friction larger than
254 0.01, a threshold that avoids capturing micro-slips before a major slip event
255 [Dorostkar *et al.*, 2017b]. The slip recurrence time and its standard deviation decreases
256 with increasing inter-particle friction coefficient, meaning that slip events occur more
257 often and more regularly in a gouge with higher frictional particles (Fig. 3c)

258 To complement the observations in Fig. 3, in Fig. 4a, we observe an almost linear
259 relation between macroscopic friction and gouge thickness for simulations with
260 different inter-particle friction coefficient. The more dense population of data points
261 at higher thickness and macroscopic friction is consistent with the nonlinear behavior
262 observed in Figs. 2b and 2c. We also observe that the number of slip events increases
263 with increasing inter-particle coefficient (equivalent to a decreasing recurrence time
264 as seen in figure 3c) The histogram of slip events' friction drop (Fig. 5) shows that

265 this increase in number of events at higher inter-particle friction coefficient mainly
266 stems from smaller events: a fault gouge with higher inter-particle friction coefficient
267 experiences more smaller slip events at a shorter and more regular inter-event time
268 (less standard deviation in Fig. 3c) with lower friction (stress) drop. Remark however
269 that, at high inter-particle friction, although the majority of the slip events are smaller,
270 there are also some extreme slip events, which are larger than the events at lower
271 inter-particle friction.

272 When studying the time evolution of the average contact force, we interestingly
273 find a similar stick-slip type of behavior (Fig. 6). This observation shows that the
274 macroscopic response of the sheared granular gouge is controlled by the contact
275 forces at grain scale, i.e. by its grain scale behavior. We observe that, by increasing
276 the inter-particle friction coefficient, the average contact force increases, however
277 the relative increase of higher inter-particle friction coefficient becomes smaller at
278 higher values. The decomposition of contact force into normal and tangential
279 components shows that the contribution of the normal component is dominant
280 irrespective of inter-particle friction coefficient. The relative contribution of normal
281 contact force to the total contact force compared to the contribution of the tangential
282 contact force decreases for higher inter-particle frictions. This means that, despite a
283 small increase in tangential contact force, the overall enhanced shear strength of fault
284 gouge (higher macroscopic friction) at higher inter-particle friction coefficient cannot
285 solely stem from the increase of tangential contact force. In other words, although
286 the inter-particle friction coefficient is not directly contributing to the normal contact

287 force, its increase results in a higher normal contact force enhancing the shear
288 capacity of the system. The hypothesis is that, there exists a structural effect where
289 at higher inter-particle coefficient less slipping contacts occur, providing a better
290 support for a contact network to build up higher contact forces. Indeed, when
291 studying the slipping contact ratio (SCR), which is defined as the ratio between
292 number of contacts at Coulomb frictional limit prone to slip and the total number
293 of contacts, we observe drops in SCR of almost one order of magnitude when
294 changing the inter-particle friction from 0.1 to 0.5 or from 0.5 to 0.9 (Fig. 7a). At the
295 same time, Fig. 7b shows that the average coordination number (coordination
296 number is the number of contacts per particle) decreases with increasing particle
297 friction coefficient. The decrease in coordination number for higher inter-particle
298 frictions can be attributed to the larger dilation or higher gouge thickness (see Fig.
299 2b). We remark that, since the coordination number decreases with increasing inter-
300 particle friction coefficient (Fig. 7b), we also check the total number of slipping
301 contacts that is not normalized by the number of contacts and observe similar
302 behavior: the total number of slipping contacts decreases with increasing particle
303 friction coefficient.

304 In Figs. 7c and 7d, we show the instantaneous and cumulative particle
305 displacement averaged over all particles, respectively. The instantaneous particle
306 displacement shows larger jumps upon micro- or major slips for higher inter-particle
307 friction coefficients. Moreover, the cumulative particle displacement clearly shows
308 that for a given instant in time (or a given shear strain), particles with higher inter-

309 particle friction underwent higher total displacements. The cumulative displacement
310 is the total displacement of a particle from the start of each simulation. Our analysis
311 shows that particle displacement is mainly in x-direction (99 %) along the moving
312 boundary that imposes the shear stress (Fig. 1).

313 We also study the evolution of potential and kinetic energies in sheared granular
314 fault gouge (Fig. 8). The elastic strain potential energy is stored within the particle-
315 particle contacts through overlap between particles [*Dorostkar & Carmeliet, 2018*] and
316 the kinetic energy is due to translation and rotation of particles. The fault gouge with
317 higher inter-particle friction coefficient shows more potential energy, however, the
318 increase in average potential energy is not linear with the increase of inter-particle
319 friction. For instance, an increase of friction coefficient by a factor 9, from 0.1 (Fig.
320 8c) to 0.9 (Fig. 8a), leads to an increase in potential energy only by a factor 3. We also
321 observe that the kinetic energy signal for higher inter-particle frictions shows more
322 fluctuations and bursts i.e. indicating important rearrangements of particles inside
323 the fault gouge. While the potential energy at low inter-particle friction coefficient
324 (Fig. 8c) shows a plateau before the major slip events, the energy is always increasing
325 approaching slip events for higher inter-particle frictions (Fig. 8a).

326 We compare in Fig. 9 the evolution of macroscopic friction and gouge thickness
327 for inter-particle friction coefficients with 2 orders of magnitude contrast i.e. 10, 1
328 and 0.1. The nucleation phase of slip events for higher inter-particle friction
329 coefficient (Fig.9a) shows a complex behavior in both macroscopic friction and
330 gouge thickness signals, where a considerable amount of small drops in friction

331 coefficient occur during the stick phase before an upcoming extreme slip event that
332 has a long recurrence time. The statistical analysis of the size of all slip events based
333 on drop in macroscopic friction (Fig. 10) shows that slip events occur more often
334 for higher inter-particle friction coefficients i.e. larger number of slip events with
335 shorter recurrence interval. More importantly, we observe that, although the higher
336 number of slip events stems mainly from smaller events (see also Fig. 5), there exist
337 also some very large slip (extreme) events (Fig. 10).

338 A commonly used technique to monitor fault activity in experiments is Acoustic
339 Emission (AE) [McLasky & Glaser, 2011; Goebel et al., 2012; Johnson et al., 2013; Goebel
340 et al., 2014b; Goebel et al., 2017; Rivière et al., 2018]. The origin of AE during laboratory
341 stick-slip experiments is still under debate, where the AE is suggested to originate
342 from groaning, creaking, and chattering of continuous grain motions and breakage
343 of force chains within the fault gouge [Rouet-Leduc et al., 2017; Rivière et al., 2018]. Our
344 analyses in this study show that the velocity (or acceleration) signal of a flagged
345 particle demonstrates a very similar behavior to acoustic data of the lab (Fig. 11a),
346 containing similar information for the prediction of macroscopic friction signal (e.g.
347 [Rouet-Leduc et al., 2017]). However, since the velocity profile of a flagged particle
348 contains both motion from arriving waves owing to rearrangements of other particles
349 and the motion of the particle itself, we call it “pseudo AE” signal. In other words,
350 although our AE signal is derived from the motion of a single, flagged particle
351 compared to the lab signal where the AE is usually reordered with a device outside
352 of the fault gouge; we find that the pseudo AE signal contains sufficient information

353 for the purpose of this study, where we compare the velocity signal from the same
354 particles for simulations with different inter-particle friction coefficient. The velocity
355 signal shows bursts at slip events, which are larger for higher inter-particle
356 coefficients (Fig. 11b). The complementary Cumulative Distribution Function
357 (cCDF) of pseudo acoustic emission bursts (for all emissions without threshold,
358 during both stick and slip phases) in Fig. 12 clearly shows the increase of AE
359 amplitude for higher inter-particle friction coefficients. We remark that the
360 observations in Fig. 11 and 12 are not dependent on the flagged particle and are
361 consistently recorded for several chosen particles.

362 We further look at the micromechanics of fault by visualizing the particles on a
363 plane representative of the whole box (here the front plane of the gouge) for inter-
364 particle friction coefficients of 0.1 and 10, at a point during the stick phase (Fig. 13).
365 For panels a and b, we set the maximum of color bar equal to the shear driving plate
366 velocity, 0.06 cm/s. While a gradient is observed for inter-particle friction of 0.1 from
367 top to bottom with particles close to the bottom plate having velocity close to 0.06
368 cm/s, the particle velocity field shows a more uniformly distributed profile for inter-
369 particle friction of 10. We will discuss the implications of this observation in Section
370 4. A comparison between panels c and d shows a larger cumulative displacement for
371 particles with inter-particle friction of 10, where the maximum of color bar is set to
372 the maximum cumulative displacement of particles with inter-particle friction of 0.1,
373 for a better comparison. It is clear from Fig. 13d that a larger portion of the sample
374 has experienced a large displacement. We remind that the main displacement for

375 particles is in x direction, along the driving plate motion. The spatial distributions in
376 panels c and d are consistent with temporal evolution in Fig. 7d. The spatial
377 distributions of coordination number for both inter-particle friction coefficients are
378 rather uniform, while the gouge with lower inter-particle friction shows higher
379 coordination numbers consistent with observations of Fig. 7b. The gouge with
380 higher inter-particle friction shows on average lower numbers, also showing some
381 'blue' spots with low coordination number.

382 **4- Discussion**

383 We discuss our main findings and present them in the frame of comparison with
384 other recent studies on the impact of inter-particle friction coefficient as well as fault
385 surface roughness. The maximum macroscopic friction coefficient (or frictional
386 strength of the sheared granular fault gouge) during stick-slip dynamics increases
387 with inter-particle friction coefficient representing the particle roughness, but
388 saturates at inter-particle friction values around 0.9-1 (Fig. 3). This observation is
389 similar to previous studies on peak shear strength of granular materials as well as
390 stable sliding of a sheared granular layer, where the nonlinear macroscopic behavior
391 and saturation of friction are observed and attributed to rotation of particles [J.
392 *Latham et al., 2005; Azéma et al., 2012; Shojaee et al., 2012; Göncü & Luding, 2013;*
393 *Rathbun et al., 2013; Azéma et al., 2017*]. Knuth and Marone [2007] also observed a
394 systematic relationship between the strength of granular layers and the surface
395 roughness of particles [Knuth & Marone, 2007]. Rough faults are suggested to
396 undergo more deformation in the fault zone requiring more overall work to shear

397 the fault [Rathbun *et al.*, 2013], as we also observe in the higher cumulative particle
398 displacement for fault gouge with higher particle roughness (Fig. 7 and Fig. 13).
399 Furthermore, we show a linear relation between macroscopic stick-slip friction and
400 gouge thickness (Fig. 4), as is confirmed by previous research [Mead, 1925; Marone,
401 1998b; Frye & Marone, 2002; Knuth & Marone, 2007; Makedonska *et al.*, 2011].

402 The macroscopic frictional strength of a granular layer also follows the bulk
403 properties (e.g. bulk stiffness) [Rabinowicz, 1956; Knuth & Marone, 2007; Leeman *et al.*,
404 2016]. It is suggested that particle-scale roughness is responsible for enhancing the
405 elasticity of a granular system at global scale [Wang *et al.*, 2007]. Similarly, we also
406 observe in Fig. 6 that the higher particle roughness makes a granular structure
407 stronger, which is capable of building higher contact forces leading to a higher shear
408 strength.

409 We observe higher standard deviation for both macroscopic stick-slip friction and
410 gouge thickness with increasing roughness (Fig. 3). A hypothesis here is that the fault
411 gouge with higher particle roughness has to undergo more complex states during
412 deformation towards failure, which involves more locked contacts (and less slipping
413 contacts; see Fig. 7) in spite of a lower total number of contacts, which makes the
414 system to experience a wider range of macroscopic frictions and dilations manifested
415 in higher variability of friction coefficient and gouge thickness (Fig. 3). The system
416 with rougher particle surface going through those complex topographical states has
417 to expand more to accommodate the continuous externally applied shear, which
418 leads to a higher dilatation and a lower coordination number. These conditions make

419 a fault gouge with rougher particle surface to fail more frequently leading to more
420 fluctuations and variability both in macroscopic friction (slip events) and gouge
421 thickness. Slip events in a sheared granular layer are reported as a collective
422 phenomenon: slipping contact ratio increases approaching the failure leading to a
423 major slip event. Therefore, from another point of view, in a system with a higher
424 particle roughness and lower slipping contact ratio, the slip event is prevented due
425 to stronger contacts, so that the system fails only partially leading to a large number
426 of small slips. We also remark that, since the main displacement for particles is along
427 the direction of the shear driving plate (x direction in Fig. 1), the higher cumulative
428 particle displacement is consistent with a higher number of slip events, where at each
429 slip event there is a displacement (rupture) for the center of mass of the granular
430 fault gouge.

431 The recent numerical model using 2-D plane strain calculations by Tal and Hager
432 [2018] showed that, as the roughness amplitude increases, the load in the fault is
433 released by more slip events but with lower average stress drops [Tal & Hager, 2018].
434 Similarly, we observe in Fig. 4 that increase of particle roughness leads to more slip
435 events but with lower friction drops. Using numerical simulations, Tal et al. [2018]
436 observed a more complex behavior for faults with higher roughness, where the
437 complexities in the nucleation process are reflected as irregular fluctuations in the
438 moment rate for rougher faults [Tal et al., 2018]. Interestingly, we observe a similar
439 complexity in 3D DEM, where the nucleation (stick) phase of slip events contains
440 many fluctuations i.e. smaller slip events. However, using the advantage of DEM and

441 employing the periodic boundary conditions we can, in contrast to experiments,
442 shear the fault gouge during long time collecting information of hundreds of slip
443 events. Using a statistical analysis, we then show that a fault gouge with high enough
444 particle roughness and large enough shear displacement shows, besides the large
445 amount of small events, some extreme slip events with long recurrence time
446 compared to faults with lower roughness.

447 Previous research on continuous monitoring of AE during stick-slip experiments
448 of rocks has deepened our understanding from the micromechanics of slip events
449 [McLasky & Glaser, 2011; Goebel et al., 2012]. The experimental work by Kwiatek et
450 al. [2014] showed that the observed changes in AE characteristics are clearly
451 correlated to the fault topography and roughness [Kwiatek et al., 2014]. Goebel et al.
452 [2017] showed that faults with rougher surface show a more spatially distributed AE
453 activity and a higher b-value [Goebel et al., 2017]. Our DEM simulations also show
454 dependency of AE on fault particle roughness. We observe higher temporal (Fig. 11
455 and 12) and more spatially distributed AE (Fig. 13) for higher fault particle
456 roughness. The higher AE in fault gouge with higher particle surface roughness is
457 consistent with more frequent kinetic energy releases (Fig. 8), since AE is believed
458 to originate from the rearrangement of particles. We remind that, although our
459 discussion on AE is based on velocity tracking of single flagged particles (called here
460 pseudo AE), the temporal evolution and higher moments of those signals show very
461 similar behavior to laboratory AE (e.g. [Rouet-Leduc et al., 2017; Rivière et al., 2018]), as
462 we are using them for machine learning analyses in our ongoing research.

463 Overall, our observations on the effect of particle roughness approximated by inter-
464 particle friction coefficient using 3-D DEM model of a granular fault gouge show
465 similarities to other numerical and experimental works on the effect of fault surface
466 roughness that did not consider the granular gouge. The DEM model in this work is
467 a vast simplification of real faults in nature but yet expands our understanding of
468 micro-scale fault roughness and provides a mean to study and measure quantities
469 that are not feasible to measure in the lab and in the field, showing how numerical
470 models can boost our understanding from physical process that dictate frictional
471 strength of a fault damage zone.

472 **5- Conclusions**

473 We model stick-slip dynamics of a granular fault gouge by 3-D discrete element
474 simulations for different values of the micro-scale fault roughness (referred to as
475 particle roughness) approximated by the inter-particle friction coefficient to better
476 understand its effect on the characteristics of seismic cycles. The major findings of
477 this study can be summarized as follows:

- 478 - The fault gouge frictional strength, dilation and their standard deviation
479 nonlinearly increase with the particle roughness, saturating at high inter-
480 particle friction.
- 481 - The average slip events' recurrence time and its standard deviation decreases
482 with particle roughness, meaning that, rougher faults fail more frequently. A
483 rougher fault shows a more complex nucleation (stick) phase, characterized

484 by many small slip events as manifested by the more frequent energy release
485 in the kinetic energy signal.

486 - Our statistical analyses on a large number of slip events obtained by shearing
487 the fault gouge to a large shear strain show that rougher faults show a higher
488 number of slip events mainly consisting in small slip events (small drops in
489 friction coefficient), however there are also some extreme slip events larger
490 than the extreme events of smoother faults.

491 - The fault gouge with higher particle roughness shows higher stored potential
492 energy and stronger particle-particle contacts, a structure that needs more
493 work to deform it and therefore, for a given shear strain, the particles
494 experience more deformation.

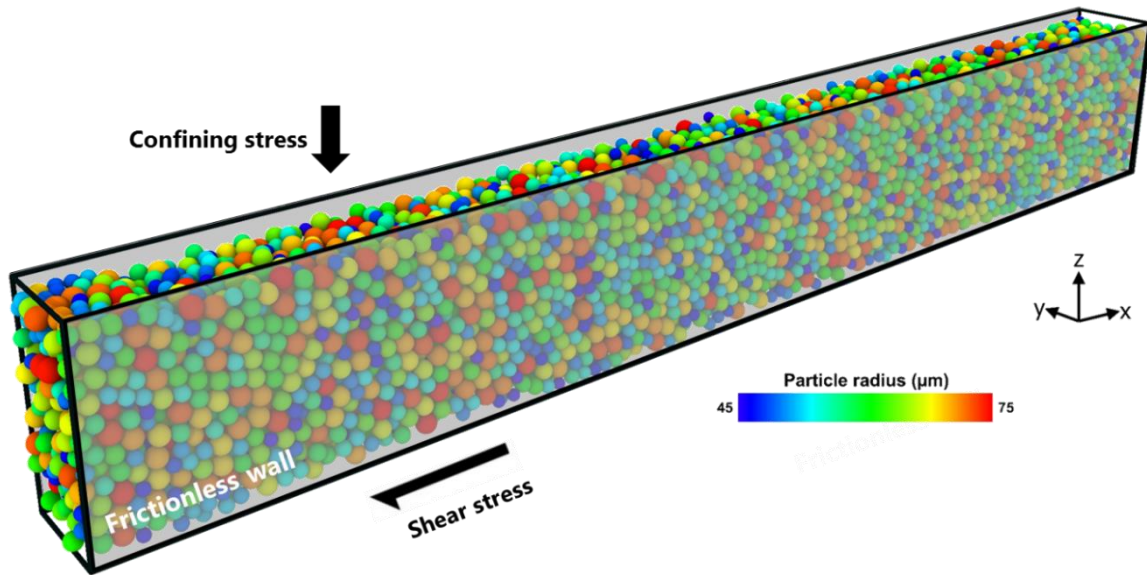
495 - The pseudo acoustic emission analysis, based on the monitoring of the
496 velocity of particles, shows higher temporal AE for fault gouge with higher
497 particle surface roughness.

498 **6- Acknowledgement**

499 The authors thank ETH Zurich for funding this study. The data related to this paper
500 can be obtained by contacting the corresponding author at domid@ethz.ch.

501 7- Figures

502



503

504

505

506 **Fig. 1:** Three dimensional granular fault gouge with 8000 particles with poly-disperse
507 diameter distribution of 90-150 micrometer. The fault gouge is confined in z
508 direction and sheared in x direction with periodic boundary conditions (Image
509 produced with the open source visualization tool (OVITO) [Stukowski, 2010]).

510

511

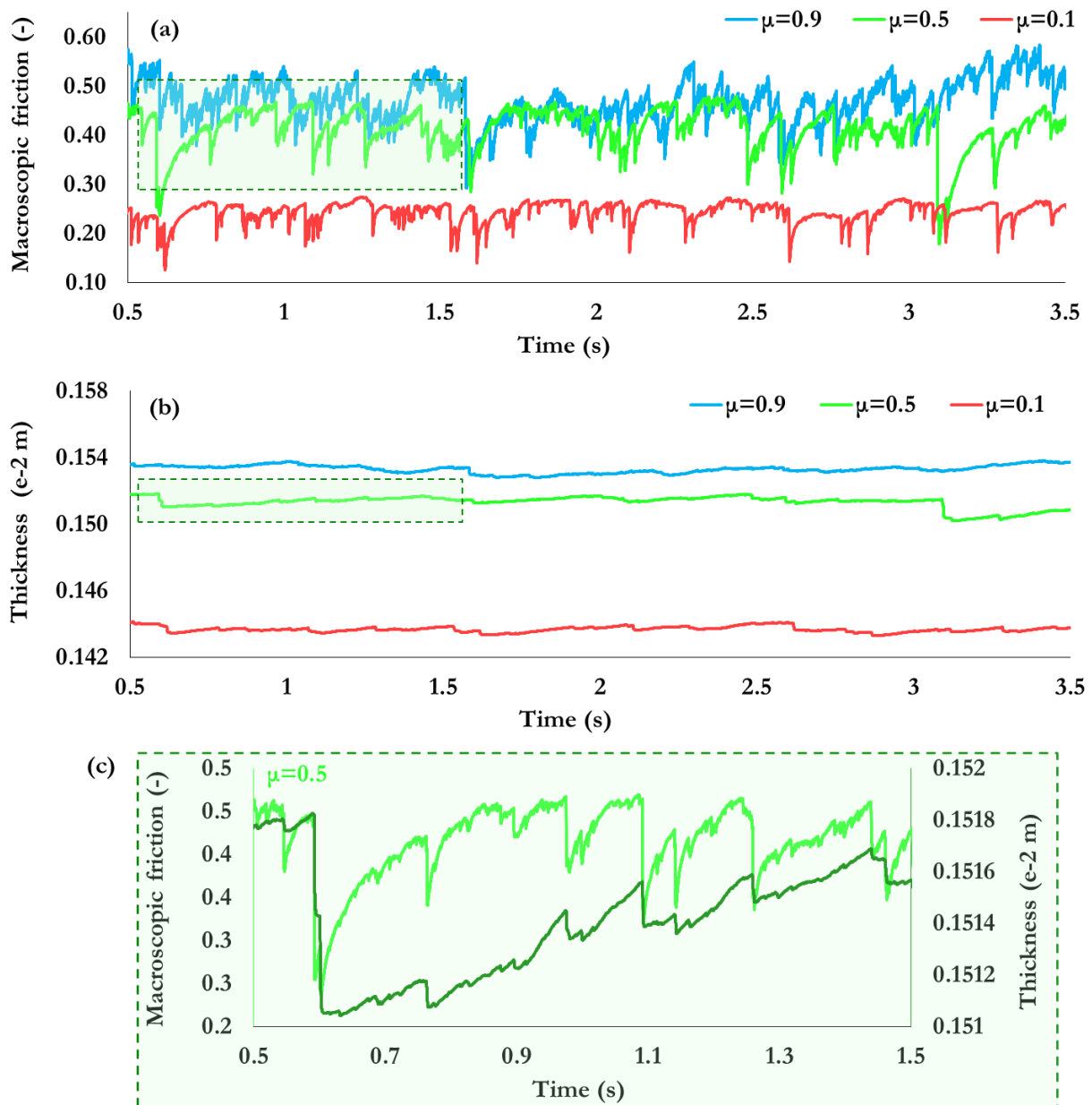
512

513

514

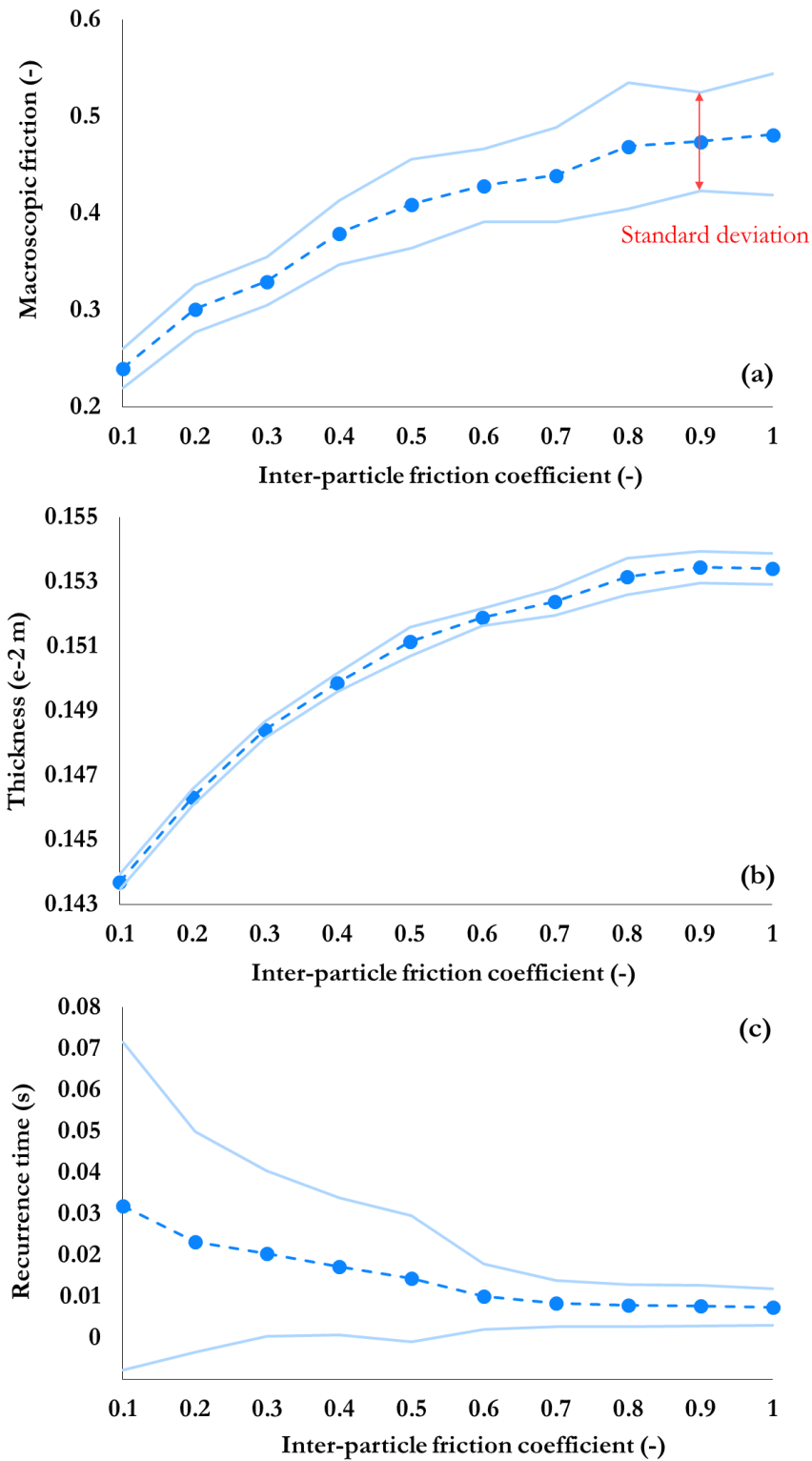
515

516



517
 518 **Fig. 2:** Time series of (a) macroscopic friction and (b) fault gouge thickness for three
 519 different inter-particle friction coefficients. The greenish shaded areas in a and b are
 520 shown in (c) with a higher resolution for $\mu = 0.5$. Please note that the thickness is
 521 shown with a secondary axis in c.

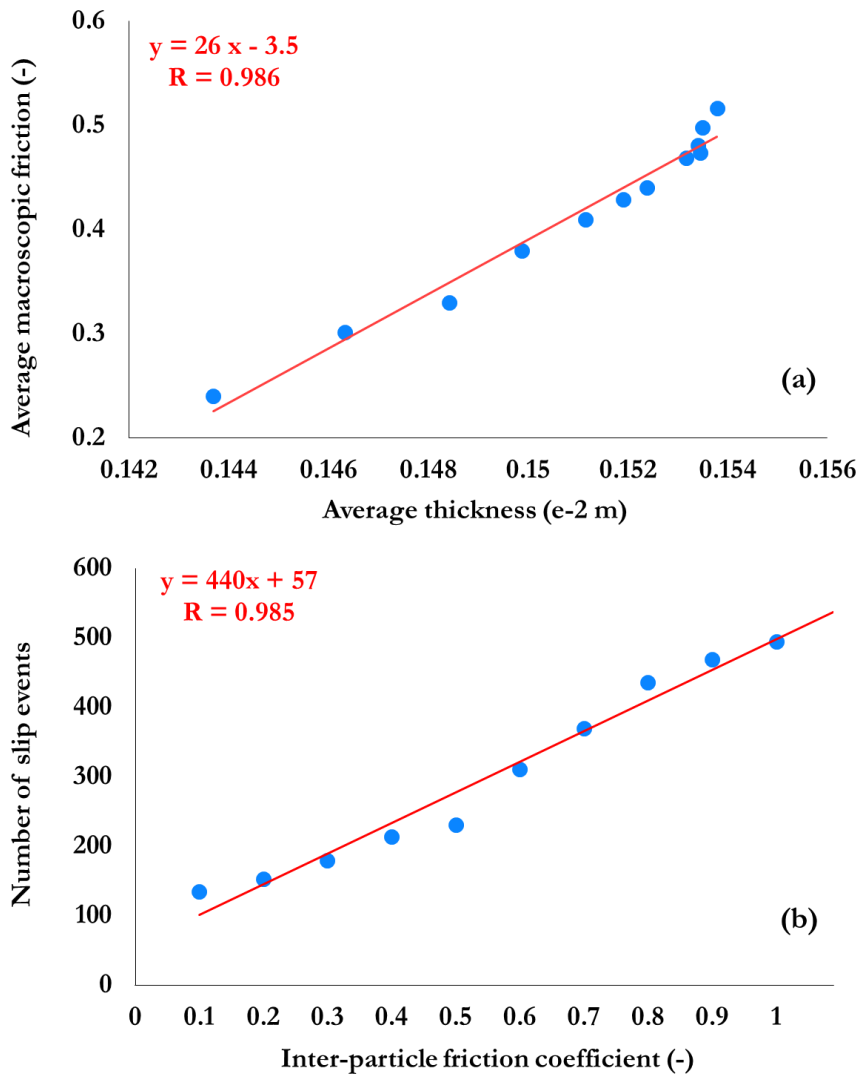
522
 523
 524



525

526

527 **Fig. 3:** Average (a) macroscopic friction, (b) fault gouge thickness and (c) slip
 528 recurrence time for long time-train stick-slip dynamics as function of the inter-
 529 particle friction coefficient. The light blue line in each image shows the uncertainty
 530 limits based on the standard deviation of data.

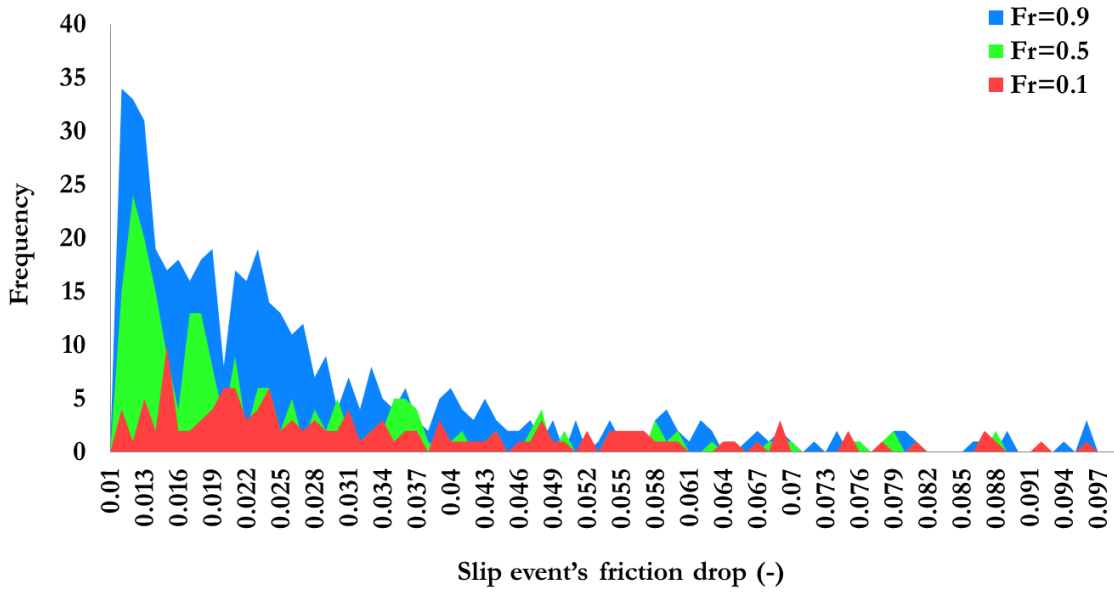


531

532 **Fig. 4:** (a) Average macroscopic friction versus average thickness for stick-slip
 533 dynamics with different inter-particle friction coefficients. (b) Number of slip events
 534 versus inter-particle friction coefficient.

535

536

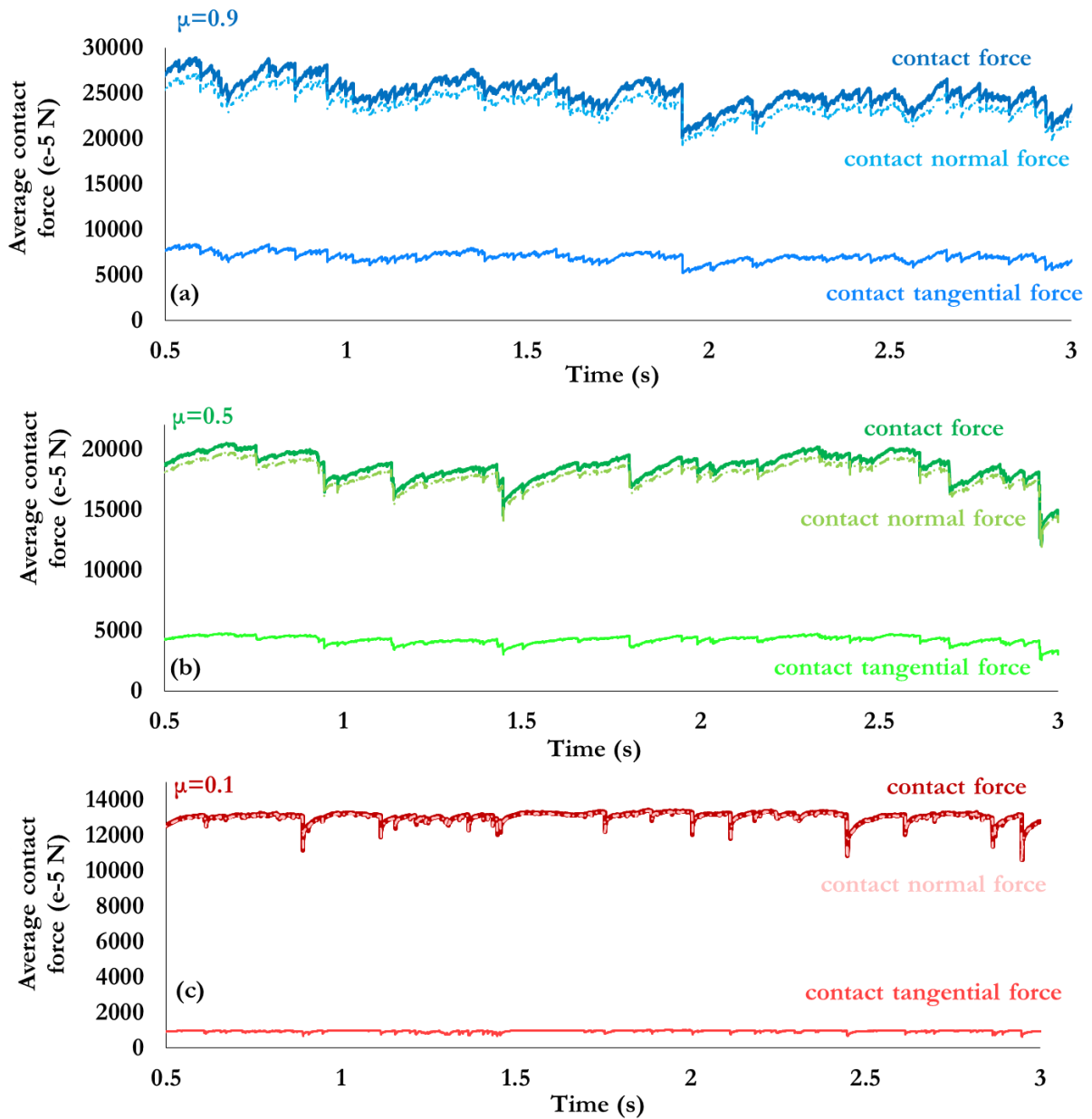


537

538

539 **Fig. 5:** Histogram of slip event's friction drop for three different inter-particle
 540 friction coefficients. The maximum slip event's friction drop in this histogram is
 541 limited to 0.1 to highlight and better show the frequency of slip events with small
 542 friction drop.

543



544

545 **Fig. 6:** (a-c) Average contact force for inter-particle friction coefficients of 0.1, 0.5
 546 and 0.9, respectively. In each panel, the components of contact force (normal contact
 547 force and tangential contact force) are separately shown.

548

549

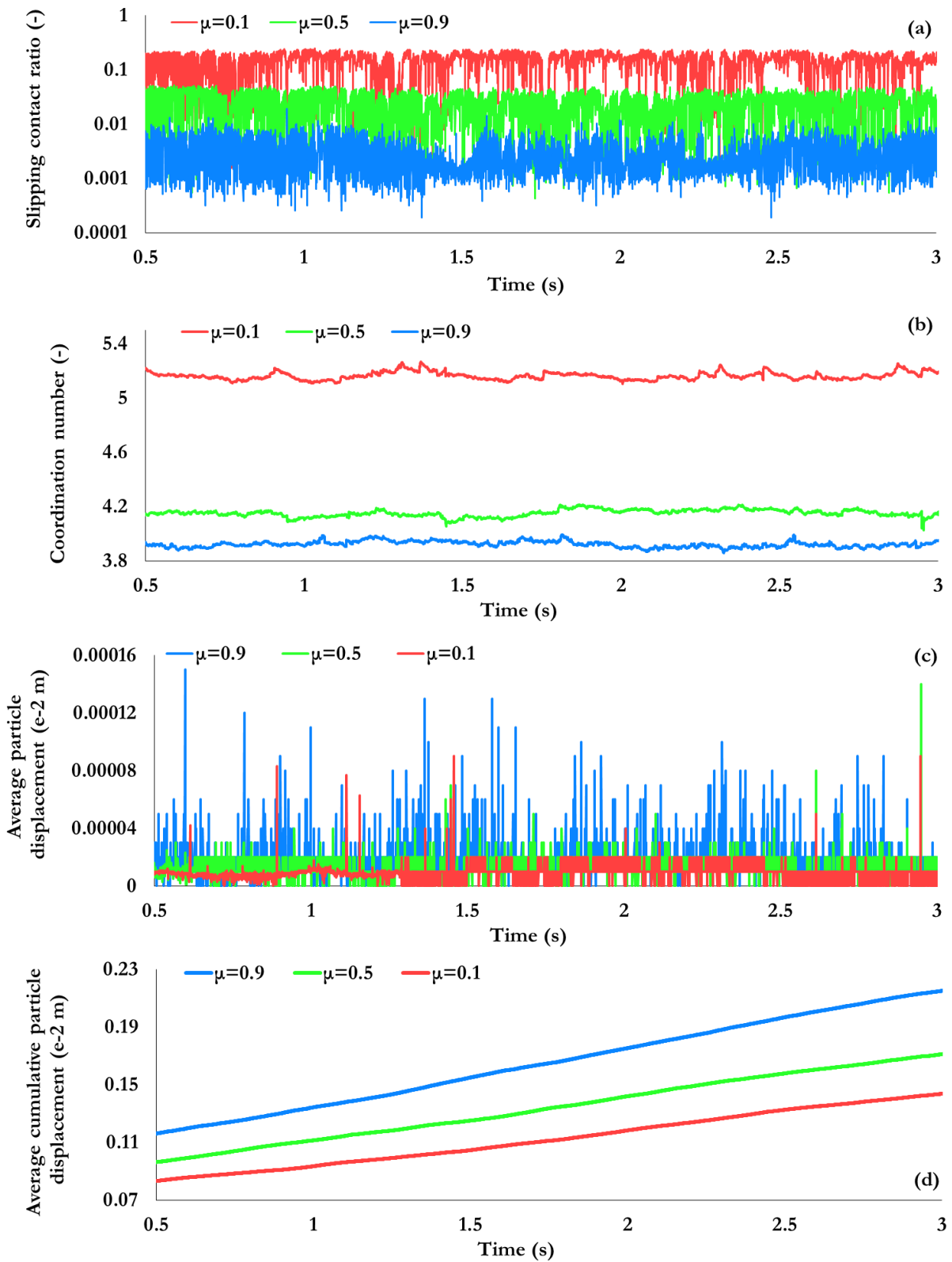
550

551

552

553

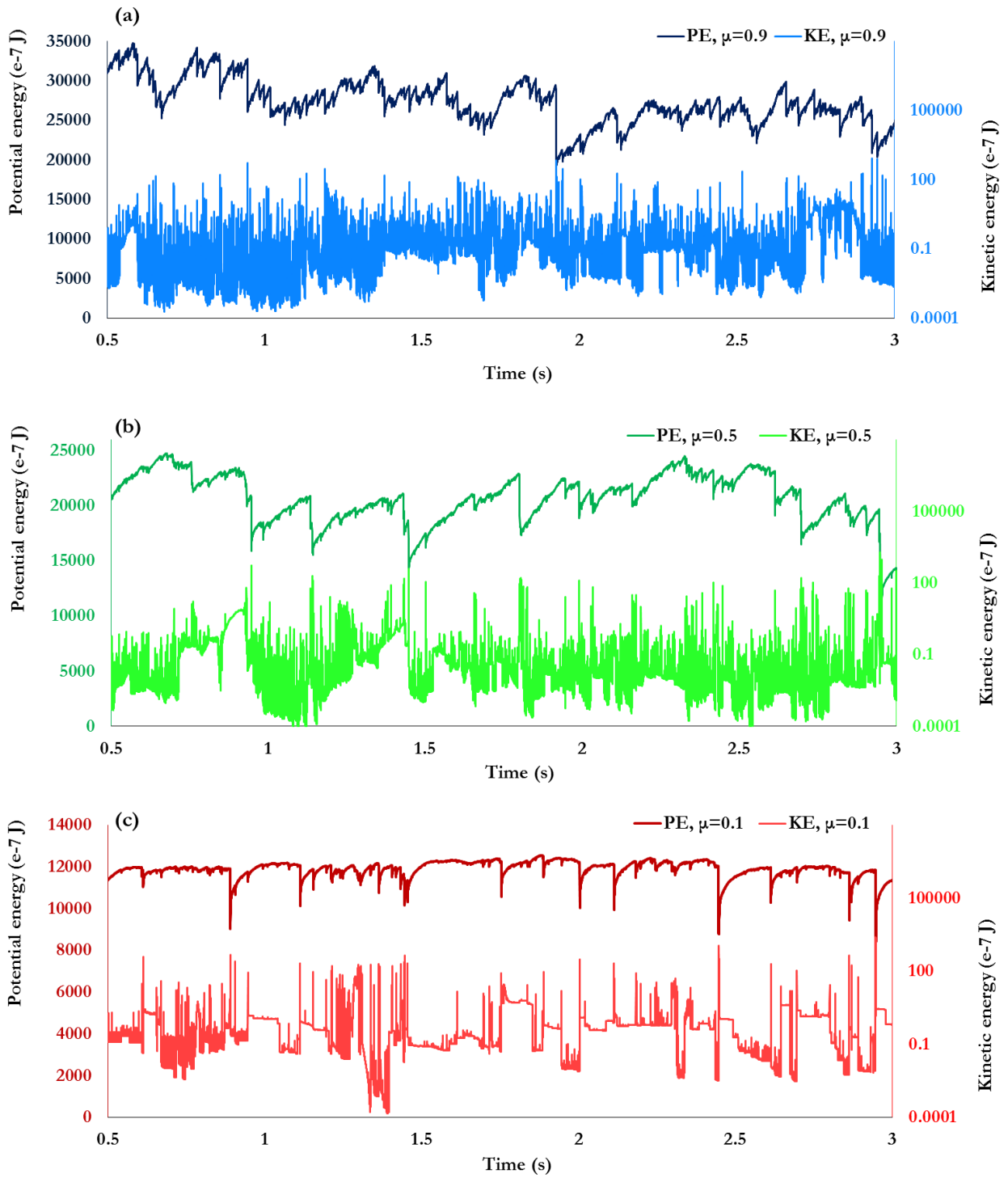
554



555

556 **Fig. 7:** Time series of (a) slipping contact ratio, (b) coordination number, (c) average
 557 particle displacement and (c) average cumulative particle displacement for inter-
 558 particle friction coefficients of 0.1, 0.5 and 0.9.

559

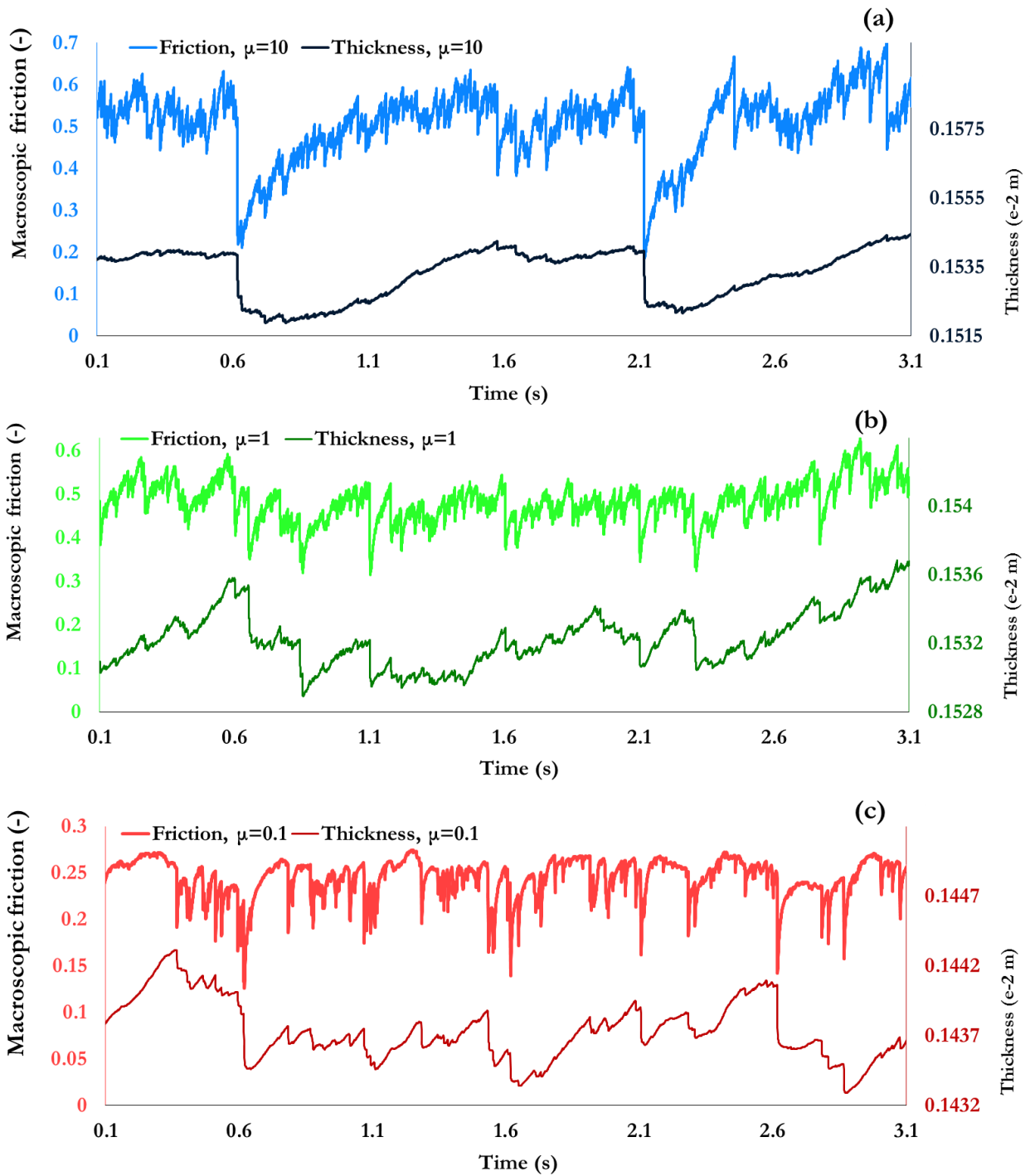


560

561 **Fig. 8:** (a-c) Evolution of potential energy (primary axis, left) and kinetic energy
 562 (secondary logarithmic axis, right) for inter-particle friction coefficients of 0.9, 0.5
 563 and 0.1, respectively.

564

565



566

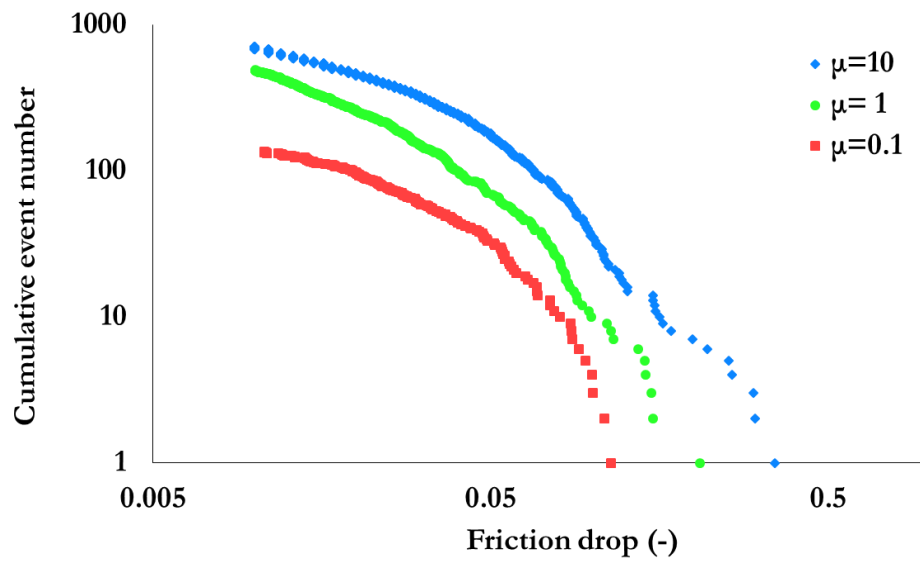
567

568 **Fig. 9:** (a-c) Time series of macroscopic friction (primary axis, left) and gouge
 569 thickness (secondary axis, right) for inter-particle friction coefficients of 10, 1, 0.1
 570 respectively.

571

572

573



574

575

576 **Fig. 10:** Cumulative number of slip events versus friction coefficient drop for
 577 different inter-particle friction coefficients of 10, 1 and 0.1.

578

579

580

581

582

583

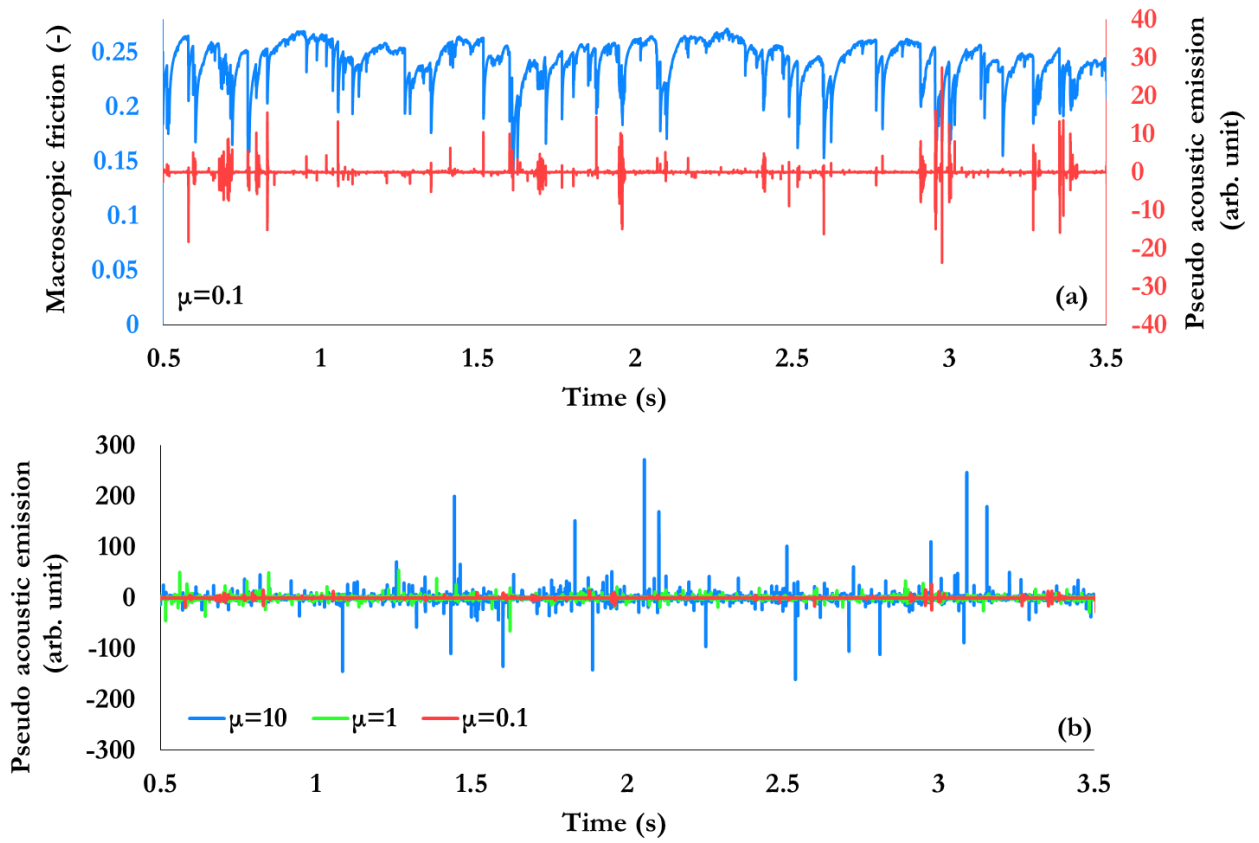
584

585

586

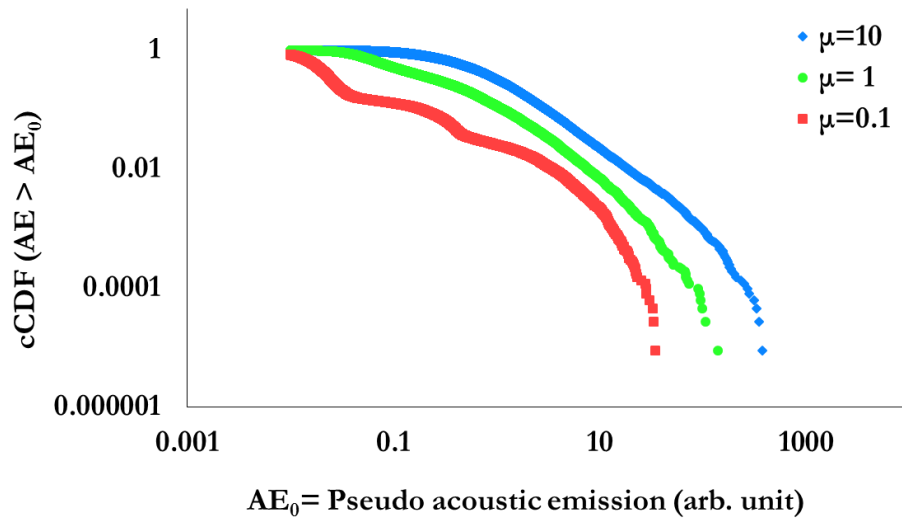
587

588



589
 590
 591
 592
 593
 594
 595
 596
 597
 598
 599
 600
 601
 602
 603

Fig. 11: (a) Friction coefficient (primary axis, left) and pseudo acoustic emission (secondary axis, right) for inter-particle friction coefficients of 10, 1 and 0.1. (b) Time series of pseudo acoustic emission for inter-particle friction coefficients of 10, 1 and 0.1.



604

605 **Fig. 12:** Complementary Cumulative Distribution Function of pseudo acoustic
 606 emission for different inter-particle friction coefficients of 10, 1 and 0.1.

607

608

609

610

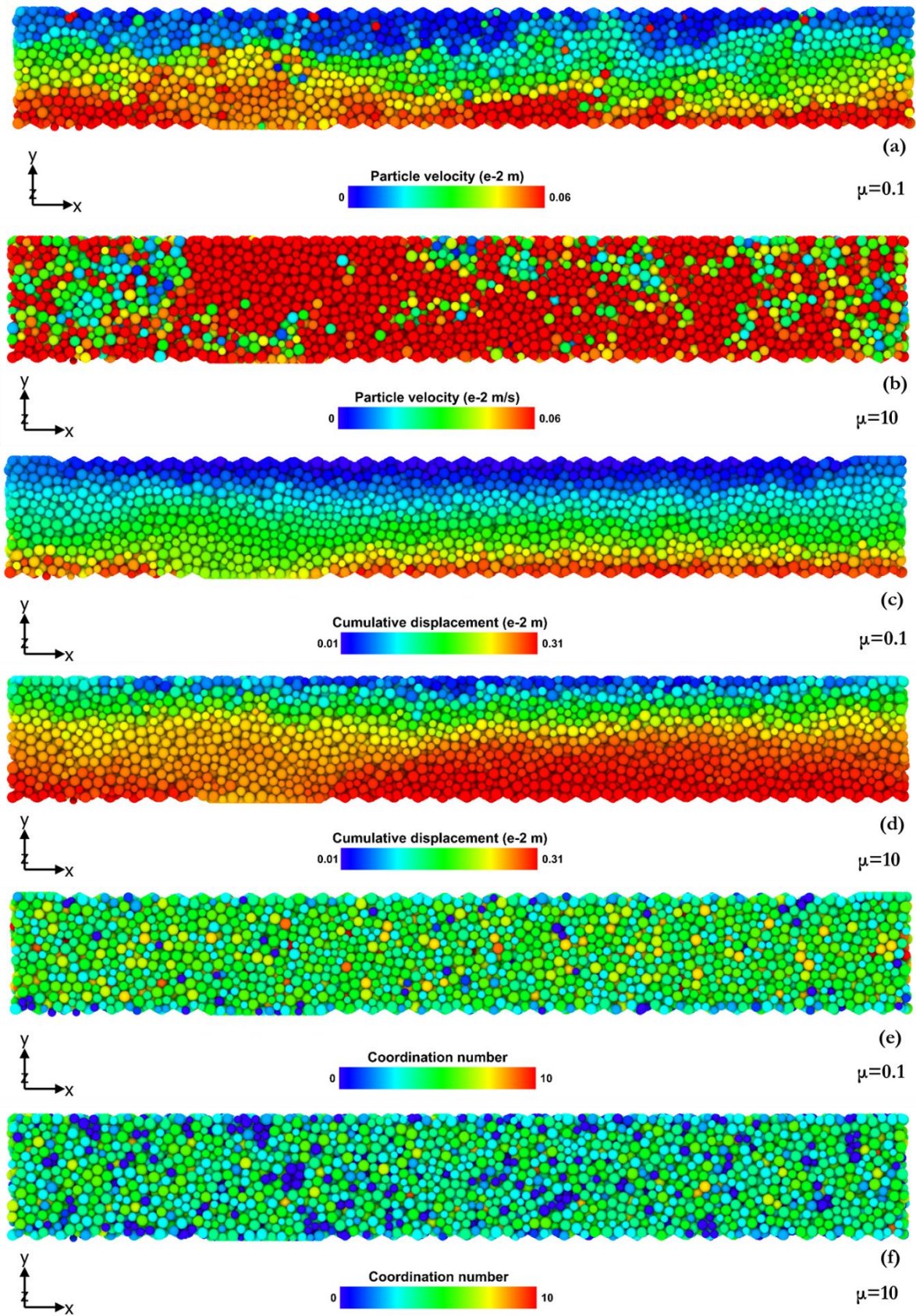
611

612

613

614

615



616

617 **Fig. 13:** (a, c, e) Spatial distribution of particle velocity, cumulative displacement and
 618 coordination number for inter-particle friction coefficients of 0.1 and (b, d, f) for
 619 inter-particle friction coefficient of 10, respectively.

8- References

- 620
621
622 Agnolin, I., & Roux, J. N. (2007). Internal states of model isotropic granular packings.
623 I. Assembling process, geometry, and contact networks. *Phys. Rev. E*, 76(6).
624 doi:10.1103/PhysRevE.76.061302
- 625 Angheluta, L., Candela, T., Mathiesen, J., & Renard, F. (2011). Effect of surface
626 morphology on the dissipation during shear and slip along a rock–rock
627 interface that contains a visco-elastic core. *Pure Appl. Geophys.*, 168(12), 2335-
628 2344. doi:10.1007/s00024-011-0272-8
- 629 Anthony, J. L., & Marone, C. (2005). Influence of particle characteristics on granular
630 friction. *J. Geophys. Res.*, 110(B8). doi:10.1029/2004jb003399
- 631 Azéma, E., Estrada, N., Preechawuttipong, I., Delenne, J.-Y., & Radjai, F. (2017).
632 Systematic description of the effect of particle shape on the strength
633 properties of granular media. *EPJ Web Conf.*, 140, 06026.
- 634 Azéma, E., Estrada, N., & Radjaï, F. (2012). Nonlinear effects of particle shape
635 angularity in sheared granular media. *Phys. Rev. E*, 86(4), 041301.
636 doi:10.1103/PhysRevE.86.041301
- 637 Biegel, R. L., Sammis, C. G., & Dieterich, J. H. (1989). The frictional properties of a
638 simulated gouge having a fractal particle distribution. *J. Struct. Geol.*, 11(7), 827-
639 846. doi:https://doi.org/10.1016/0191-8141(89)90101-6
- 640 Bistacchi, A., Griffith, W. A., Smith, S. A. F., Di Toro, G., Jones, R., & Nielsen, S.
641 (2011). Fault roughness at seismogenic depths from lidar and
642 photogrammetric analysis. *Pure Appl. Geophys.*, 168(12), 2345-2363.
643 doi:10.1007/s00024-011-0301-7
- 644 Bouchon, M., Karabulut, H., Bouin, M.-P., Schmittbuhl, J., Vallée, M., Archuleta, R.,
645 . . . Marsan, D. (2010). Faulting characteristics of supershear earthquakes.
646 *Tectonophysics*, 493(3), 244-253.
647 doi:https://doi.org/10.1016/j.tecto.2010.06.011
- 648 Brantut, N., Schubnel, A., Rouzaud, J. N., Brunet, F., & Shimamoto, T. (2008). High-
649 velocity frictional properties of a clay-bearing fault gouge and implications for
650 earthquake mechanics. *J. Geophys. Res.*, 113(B10). doi:10.1029/2007JB005551

- 651 Brodsky, E. E., Gilchrist, J. J., Sagy, A., & Collettini, C. (2011). Faults smooth
652 gradually as a function of slip. *Earth Planet. Sci. Lett.*, *302*(1), 185-193.
653 doi:<https://doi.org/10.1016/j.epsl.2010.12.010>
- 654 Brodsky, E. E., Kirkpatrick, J. D., & Candela, T. (2016). Constraints from fault
655 roughness on the scale-dependent strength of rocks. *Geology*, *44*(1), 19-22.
- 656 Bruhat, L., Fang, Z., & Dunham, E. M. (2016). Rupture complexity and the
657 supershear transition on rough faults. *J. Geophys. Res.*, *121*(1), 210-224.
658 doi:[doi:10.1002/2015JB012512](https://doi.org/10.1002/2015JB012512)
- 659 Candela, T., Renard, F., Bouchon, M., Brouste, A., Marsan, D., Schmittbuhl, J., &
660 Voisin, C. (2009). Characterization of fault roughness at various scales:
661 Implications of three-dimensional high resolution topography measurements.
662 *Pure Appl. Geophys.*, *166*(10), 1817-1851. doi:[10.1007/s00024-009-0521-2](https://doi.org/10.1007/s00024-009-0521-2)
- 663 Candela, T., Renard, F., Bouchon, M., Schmittbuhl, J., & Brodsky, E. E. (2011a).
664 Stress drop during earthquakes: Effect of fault roughness scaling. *Bull. Seismol.*
665 *Soc. Am.*, *101*(5), 2369-2387.
- 666 Candela, T., Renard, F., Klinger, Y., Mair, K., Schmittbuhl, J., & Brodsky, E. E.
667 (2012). Roughness of fault surfaces over nine decades of length scales. *J.*
668 *Geophys. Res.*, *117*(B8). doi:[doi:10.1029/2011JB009041](https://doi.org/10.1029/2011JB009041)
- 669 Candela, T., Renard, F., Schmittbuhl, J., Bouchon, M., & Brodsky, E. E. (2011b).
670 Fault slip distribution and fault roughness. *Geophys. J. Int.*, *187*(2), 959-968.
671 doi:[10.1111/j.1365-246X.2011.05189.x](https://doi.org/10.1111/j.1365-246X.2011.05189.x)
- 672 Cashman, S., & Cashman, K. (2000). Cataclasis and deformation-band formation in
673 unconsolidated marine terrace sand, humboldt county, california. *Geology*,
674 *28*(2), 111-114. doi:[10.1130/0091-7613\(2000\)28<111:CADFIU>2.0.CO;2](https://doi.org/10.1130/0091-7613(2000)28<111:CADFIU>2.0.CO;2)
- 675 Cashman, S. M., Baldwin, J. N., Cashman, K. V., Swanson, K., & Crawford, R.
676 (2007). Microstructures developed by coseismic and aseismic faulting in near-
677 surface sediments, san andreas fault, california. *Geology*, *35*(7), 611-614.
- 678 Chester, F. M., & Chester, J. S. (1998). Ultracataclasite structure and friction
679 processes of the punchbowl fault, san andreas system, california. *Tectonophysics*,
680 *295*(1), 199-221. doi:[https://doi.org/10.1016/S0040-1951\(98\)00121-8](https://doi.org/10.1016/S0040-1951(98)00121-8)
- 681 Chester, F. M., & Chester, J. S. (2000). Stress and deformation along wavy frictional
682 faults. *J. Geophys. Res.*, *105*(B10), 23421-23430. doi:[doi:10.1029/2000JB900241](https://doi.org/10.1029/2000JB900241)

- 683 Chester, F. M., Friedman, M., & Logan, J. M. (1985). Foliated cataclasites.
684 *Tectonophysics*, 111(1), 139-146. doi:https://doi.org/10.1016/0040-
685 1951(85)90071-X
- 686 Chester, F. M., & Logan, J. M. (1986). Implications for mechanical properties of
687 brittle faults from observations of the punchbowl fault zone, California. *Pure*
688 *Appl. Geophys.*, 124(1), 79-106. doi:10.1007/bf00875720
- 689 Di Renzo, A., & Di Maio, F. P. (2004). Comparison of contact-force models for the
690 simulation of collisions in dem-based granular flow codes. *Chem. Eng. Sci.*,
691 59(3), 525-541. doi:10.1016/j.ces.2003.09.037
- 692 Dieterich, J. H., & Kilgore, B. D. (1994). Direct observation of frictional contacts:
693 New insights for state-dependent properties. *Pure Appl. Geophys.*, 143(1), 283-
694 302. doi:10.1007/bf00874332
- 695 Dieterich, J. H., & Smith, D. E. (2009). Nonplanar faults: Mechanics of slip and off-
696 fault damage. *Pure Appl. Geophys.*, 166(10), 1799-1815. doi:10.1007/s00024-
697 009-0517-y
- 698 Dorostkar, O. (2018). *Stick-slip dynamics in dry and fluid saturated granular fault gouge*
699 *investigated by numerical simulations*. (PhD dissertation), PhD dissertation, ETH
700 Zurich.
- 701 Dorostkar, O., & Carmeliet, J. (2018). Potential energy as metric for understanding
702 stick-slip dynamics in sheared granular fault gouge: A coupled CFD–DEM study.
703 *Rock Mech. Rock Eng.* doi:10.1007/s00603-018-1457-6
- 704 Dorostkar, O., Guyer, R. A., Johnson, P. A., Marone, C., & Carmeliet, J. (2017a). On
705 the micromechanics of slip events in sheared, fluid saturated fault gouge.
706 *Geophys. Res. Lett.*, 6101–6108. doi:10.1002/2017GL073768
- 707 Dorostkar, O., Guyer, R. A., Johnson, P. A., Marone, C., & Carmeliet, J. (2017b). On
708 the role of fluids in stick-slip dynamics of saturated granular fault gouge using
709 a coupled computational fluid dynamics-discrete element approach. *J. Geophys.*
710 *Res.* doi:10.1002/2017JB014099
- 711 Dorostkar, O., Guyer, R. A., Johnson, P. A., Marone, C., & Carmeliet, J. (2018).
712 Cohesion-induced stabilization in stick-slip dynamics of weakly wet, sheared
713 granular fault gouge. *J. Geophys. Res.* doi:10.1002/2017JB015171

- 714 Dorostkar, O., Johnson, P., Guyer, R., Marone, C., & Carmeliet, J. (2017c). Do fluids
715 modify the stick-slip behavior of sheared granular media? *Poromechanics VI :
716 Proceedings of the Sixth Biot Conference on Poromechanics, 2017.* , 158-163.
717 doi:10.1061/9780784480779.019
- 718 Dunham, E. M., Belanger, D., Cong, L., & Kozdon, J. E. (2011). Earthquake ruptures
719 with strongly rate-weakening friction and off-fault plasticity, part 2: Nonplanar
720 faults. *Bull. Seismol. Soc. Am.*, *101*(5), 2308-2322.
- 721 Engelder, J. T. (1974). Cataclasis and the generation of fault gouge. *GSA Bulletin*,
722 *85*(10), 1515-1522. doi:10.1130/0016-
723 7606(1974)85<1515:CATGOF>2.0.CO;2
- 724 Faulkner, D. R., Lewis, A. C., & Rutter, E. H. (2003). On the internal structure and
725 mechanics of large strike-slip fault zones: Field observations of the carboneras
726 fault in southeastern Spain. *Tectonophysics*, *367*(3), 235-251.
727 doi:https://doi.org/10.1016/S0040-1951(03)00134-3
- 728 Ferdowsi, B. (2014). *Discrete element modeling of triggered slip in faults with granular gouge:
729 Application to dynamic earthquake triggering.* (PhD dissertation), ETH Zurich.
- 730 Fournier, T., & Morgan, J. (2012). Insights to slip behavior on rough faults using
731 discrete element modeling. *Geophys. Res. Lett.*, *39*(12).
732 doi:doi:10.1029/2012GL051899
- 733 Frye, K. M., & Marone, C. (2002). Effect of humidity on granular friction at room
734 temperature. *J. Geophys. Res.*, *107*(B11). doi:10.1029/2001jb000654
- 735 Goebel, T. H. W., Becker, T. W., Sammis, C. G., Dresen, G., & Schorlemmer, D.
736 (2014a). Off-fault damage and acoustic emission distributions during the
737 evolution of structurally complex faults over series of stick-slip events.
738 *Geophys. J. Int.*, *197*(3), 1705-1718. doi:10.1093/gji/ggu074
- 739 Goebel, T. H. W., Becker, T. W., Schorlemmer, D., Stanchits, S., Sammis, C.,
740 Rybacki, E., & Dresen, G. (2012). Identifying fault heterogeneity through
741 mapping spatial anomalies in acoustic emission statistics. *J. Geophys. Res.*,
742 *117*(B3). doi:doi:10.1029/2011JB008763
- 743 Goebel, T. H. W., Candela, T., Sammis, C. G., Becker, T. W., Dresen, G., &
744 Schorlemmer, D. (2014b). Seismic event distributions and off-fault damage
745 during frictional sliding of saw-cut surfaces with pre-defined roughness.
746 *Geophys. J. Int.*, *196*(1), 612-625. doi:10.1093/gji/ggt401

- 747 Goebel, T. H. W., Kwiatek, G., Becker, T. W., Brodsky, E. E., & Dresen, G. (2017).
748 What allows seismic events to grow big?: Insights from b-value and fault
749 roughness analysis in laboratory stick-slip experiments. *Geology*, *45*(9), 815-818.
750 doi:10.1130/G39147.1
- 751 Göncü, F., & Luding, S. (2013). Effect of particle friction and polydispersity on the
752 macroscopic stress–strain relations of granular materials. *Acta Geotech.*, *8*(6),
753 629-643. doi:10.1007/s11440-013-0258-z
- 754 Goniva, C., Kloss, C., Deen, N. G., Kuipers, J. A. M., & Pirker, S. (2012). Influence
755 of rolling friction on single spout fluidized bed simulation.
756 *PARTICUOLOGY*, *10*(5), 582-591. doi:10.1016/j.partic.2012.05.002
- 757 Haines, S., Marone, C., & Saffer, D. (2014). Frictional properties of low-angle normal
758 fault gouges and implications for low-angle normal fault slip. *Earth Planet. Sci.*
759 *Lett.*, *408*, 57-65. doi:10.1016/j.epsl.2014.09.034
- 760 Heermance, R., Shipton, Z. K., & Evans, J. P. (2003). Fault structure control on fault
761 slip and ground motion during the 1999 rupture of the chelungpu fault,
762 taiwan. *Bull. Seismol. Soc. Am.*, *93*(3), 1034-1050. doi:10.1785/0120010230
- 763 Hertz, H. (1882). Ueber die berührung fester elastischer körper. *Journal für die reine*
764 *und angewandte Mathematik*, *92*, 156-171.
- 765 Ivković, B., Djurdjanović, M., & Stamenković, D. (2000). *The influence of the contact*
766 *surface roughness on the static friction coefficient* (Vol. 22).
- 767 J. Latham, S., Abe, S., & R. Mora, P. (2005). *Macroscopic friction response of rotational and*
768 *non-rotational lattice solid gouge models in 2d and 3d*. Paper presented at the Powders
769 and Grains 2005, Stuttgart, Germany.
- 770 Johnson, P. A., Ferdowsi, B., Kaproth, B. M., Scuderi, M., Griffa, M., Carmeliet, J., .
771 . . Marone, C. (2013). Acoustic emission and microslip precursors to stick-slip
772 failure in sheared granular material. *Geophys. Res. Lett.*, *40*(21), 5627-5631.
773 doi:10.1002/2013gl057848
- 774 Johnson, P. A., & Jia, X. (2005). Nonlinear dynamics, granular media and dynamic
775 earthquake triggering. *Nature*, *437*(7060), 871-874. doi:10.1038/nature04015
- 776 Karner, S. L., & Marone, C. (2000). Effects of loading rate and normal stress on
777 stress drop and stick-slip recurrence interval. *GeoComplexity and the Physics of*
778 *Earthquakes*, 187-198.

- 779 Kloss, C., Goniva, C., Hager, A., Amberger, S., & Pirker, S. (2012). Models,
780 algorithms and validation for opensource dem and cfd-dem. *Prog. Comput.*
781 *Fluid Dyn.*, 12(2-3), 140-152.
- 782 Knuth, M., & Marone, C. (2007). Friction of sheared granular layers: Role of particle
783 dimensionality, surface roughness, and material properties. *Geochem. Geophys.*
784 *Geosyst.*, 8(3). doi:doi:10.1029/2006GC001327
- 785 Kozłowska, M., Brudzinski, M. R., Friberg, P., Skoumal, R. J., Baxter, N. D., &
786 Currie, B. S. (2018). Maturity of nearby faults influences seismic hazard from
787 hydraulic fracturing. *Proceedings of the National Academy of Sciences*, 115(8), E1720-
788 E1729. doi:10.1073/pnas.1715284115
- 789 Kwiatek, G., Goebel, T. H. W., & Dresen, G. (2014). Seismic moment tensor and b
790 value variations over successive seismic cycles in laboratory stick-slip
791 experiments. *Geophys. Res. Lett.*, 41(16), 5838-5846.
792 doi:doi:10.1002/2014GL060159
- 793 Leeman, J. R., Saffer, D. M., Scuderi, M. M., & Marone, C. (2016). Laboratory
794 observations of slow earthquakes and the spectrum of tectonic fault slip
795 modes. *Nat Commun*, 7, 11104. doi:10.1038/ncomms11104
- 796 <https://www.nature.com/articles/ncomms11104#supplementary-information>
- 797 Mair, K., Frye, K. M., & Marone, C. (2002). Influence of grain characteristics on the
798 friction of granular shear zones. *J. Geophys. Res.*, 107(B10).
799 doi:10.1029/2001jb000516
- 800 Makedonska, N., Sparks, D. W., Aharonov, E., & Goren, L. (2011). Friction versus
801 dilation revisited: Insights from theoretical and numerical models. *J. Geophys.*
802 *Res.*, 116(B9). doi:10.1029/2010jb008139
- 803 Marone, C. (1998a). The effect of loading rate on static friction and the rate of fault
804 healing during the earthquake cycle. *Nature*, 391(6662), 69-72.
805 doi:10.1038/34157
- 806 Marone, C. (1998b). Laboratory-derived friction laws and their application to seismic
807 faulting. *Annu. Rev. Earth Planet. Sci.*, 26, 643-696.
808 doi:10.1146/annurev.earth.26.1.643
- 809 Marone, C., Carpenter, B. M., & Schiffer, P. (2008). Transition from rolling to
810 jamming in thin granular layers. *Physical Review Letters*, 101(24), 248001.

- 811 Marone, C., & Kilgore, B. (1993). Scaling of the critical slip distance for seismic
812 faulting with shear strain in fault zones. *Nature*, 362, 618.
813 doi:10.1038/362618a0
- 814 Marone, C., Raleigh, C. B., & Scholz, C. H. (1990). Frictional behavior and
815 constitutive modeling of simulated fault gouge. *J. Geophys. Res.*, 95(B5), 7007-
816 7025. doi:10.1029/JB095iB05p07007
- 817 McLaskey, G. C., & Glaser, S. D. (2011). Micromechanics of asperity rupture during
818 laboratory stick slip experiments. *Geophys. Res. Lett.*, 38(12).
819 doi:doi:10.1029/2011GL047507
- 820 Mead, W. J. (1925). The geologic role of dilatancy. *The Journal of Geology*, 33(7), 685-
821 698.
- 822 MiDi, G. D. R. (2004). On dense granular flows. *Eur. Phys. J. E*, 14(4), 341-365.
823 doi:10.1140/epje/i2003-10153-0
- 824 O'Sullivan, C. (2011). *Particulate discrete element modelling: A geomechanics perspective*. Spon
825 Press.
- 826 Ohnaka, M. (2003). A constitutive scaling law and a unified comprehension for
827 frictional slip failure, shear fracture of intact rock, and earthquake rupture. *J.*
828 *Geophys. Res.*, 108(B2). doi:doi:10.1029/2000JB000123
- 829 Ohnaka, M., & Shen, L.-f. (1999). Scaling of the shear rupture process from
830 nucleation to dynamic propagation: Implications of geometric irregularity of
831 the rupturing surfaces. *J. Geophys. Res.*, 104(B1), 817-844.
832 doi:doi:10.1029/1998JB900007
- 833 Park, J.-W., & Song, J.-J. (2009). Numerical simulation of a direct shear test on a rock
834 joint using a bonded-particle model. *Int. J. Rock Mech. Min. Sci.*, 46(8), 1315-
835 1328. doi:https://doi.org/10.1016/j.ijrmms.2009.03.007
- 836 Pierre, R., S., B. H., Romain, J., & Raúl, M. (2018). Fast and slow slip events emerge
837 due to fault geometrical complexity. *Geophys. Res. Lett.*, 45(10), 4809-4819.
838 doi:doi:10.1029/2018GL077579
- 839 Rabinowicz, E. (1956). Stick and slip. *Sci. Am.*, 194(5), 109-119.

- 840 Rathbun, A. P., & Marone, C. (2010). Effect of strain localization on frictional
841 behavior of sheared granular materials. *J. Geophys. Res.*, *115*(B1).
842 doi:10.1029/2009jb006466
- 843 Rathbun, A. P., Renard, F., & Abe, S. (2013). Numerical investigation of the interplay
844 between wall geometry and friction in granular fault gouge. *J. Geophys. Res.*,
845 *118*(3), 878-896. doi:doi:10.1002/jgrb.50106
- 846 Renard, F., & Candela, T. (2017). Scaling of fault roughness and implications for
847 earthquake mechanics *Fault zone dynamic processes: Evolution of fault properties*
848 *during seismic rupture, geophysical monograph 227*: John Wiley & Sons, Inc.
- 849 Renard, F., Voisin, C., Marsan, D., & Schmittbuhl, J. (2006). High resolution 3d laser
850 scanner measurements of a strike-slip fault quantify its morphological
851 anisotropy at all scales. *Geophys. Res. Lett.*, *33*(4).
852 doi:doi:10.1029/2005GL025038
- 853 Rijsingen, E., Lallemand, S., Peyret, M., Arcay, D., Heuret, A., Funicello, F., & Corbi,
854 F. (2018). How subduction interface roughness influences the occurrence of
855 large interplate earthquakes. *Geochem. Geophys. Geosyst.*
856 doi:doi:10.1029/2018GC007618
- 857 Rivière, J., Lv, Z., Johnson, P. A., & Marone, C. (2018). Evolution of b-value during
858 the seismic cycle: Insights from laboratory experiments on simulated faults.
859 *Earth Planet. Sci. Lett.*, *482*, 407-413.
860 doi:https://doi.org/10.1016/j.epsl.2017.11.036
- 861 Rosenau, M., Corbi, F., & Dominguez, S. (2017). Analogue earthquakes and seismic
862 cycles: Experimental modelling across timescales. *Solid Earth*, *8*(3), 597-635.
863 doi:10.5194/se-8-597-2017
- 864 Rouet-Leduc, B., Hulbert, C., Lubbers, N., Barros, K., Humphreys, C. J., & Johnson,
865 P. A. (2017). Machine learning predicts laboratory earthquakes. *Geophys. Res.*
866 *Lett.*, *44*(18), 9276-9282. doi:10.1002/2017GL074677
- 867 Sagy, A., Brodsky, E. E., & Axen, G. J. (2007). Evolution of fault-surface roughness
868 with slip. *Geology*, *35*(3), 283-286. doi:10.1130/G23235A.1
- 869 Schubnel, A., Nielsen, S., Taddeucci, J., Vinciguerra, S., & Rao, S. (2011). Photo-
870 acoustic study of subshear and supershear ruptures in the laboratory. *Earth*
871 *Planet. Sci. Lett.*, *308*(3), 424-432.
872 doi:https://doi.org/10.1016/j.epsl.2011.06.013

- 873 Sheng, Y., Lawrence, C. J., Briscoe, B. J., & Thornton, C. (2004). Numerical studies
874 of uniaxial powder compaction process by 3d dem. *Eng. Computation.*, 21(2-4),
875 304-317. doi:10.1108/02644400410519802
- 876 Shimamoto, T. (1979). *Experimental studies of simulated gouge and their application to studies*
877 *of natural fault zones*. Paper presented at the Conference VIII: Analysis of Actual
878 Fault Zones in Bedrock, Natl. Earthquake Hazards Reduct. Program, Menlo
879 Park, Calif.
- 880 Shojaee, Z., Brendel, L., Török, J., & Wolf, D. E. (2012). Shear flow of dense
881 granular materials near smooth walls. Ii. Block formation and suppression of
882 slip by rolling friction. *Phys. Rev. E*, 86(1), 011302.
883 doi:10.1103/PhysRevE.86.011302
- 884 Tal, Y., & Hager, B. H. (2018). The slip behavior and source parameters for
885 spontaneous slip events on rough faults subjected to slow tectonic loading. *J.*
886 *Geophys. Res.*, 123(2), 1810-1823. doi:doi:10.1002/2017JB014737
- 887 Tal, Y., Hager, B. H., & Ampuero, J. P. (2018). The effects of fault roughness on the
888 earthquake nucleation process. *J. Geophys. Res.*, 123(1), 437-456.
889 doi:doi:10.1002/2017JB014746
- 890 Wang, K., & Bilek, S. L. (2014). Invited review paper: Fault creep caused by
891 subduction of rough seafloor relief. *Tectonophysics*, 610, 1-24.
892 doi:https://doi.org/10.1016/j.tecto.2013.11.024
- 893 Wang, W.-J., Kong, X.-Z., & Zhu, Z.-G. (2007). Friction and relative energy
894 dissipation in sheared granular materials. *Phys. Rev. E*, 75(4), 041302.
- 895 Xia, K., Rosakis, A. J., & Kanamori, H. (2004). Laboratory earthquakes: The sub-
896 rayleigh-to-supershear rupture transition. *Science*, 303(5665), 1859-1861.
897 doi:10.1126/science.1094022
- 898 Zielke, O., Galis, M., & Mai, P. M. (2017). Fault roughness and strength
899 heterogeneity control earthquake size and stress drop. *Geophys. Res. Lett.*, 44(2),
900 777-783. doi:doi:10.1002/2016GL071700
- 901 Zoback, M., Hickman, S., & Ellsworth, W. (2010). Scientific drilling into the san
902 andreas fault zone. *Eos, Transactions American Geophysical Union*, 91(22), 197-
903 199.

904